Electronic Supplementary Material (ESI) for Energy & Environmental Science.
This journal is © The Royal Society of Chemistry 2020

Electronic Supplementary Information

for

pH Swing Cycle for CO_2 Capture Electrochemically Driven through Proton-Coupled Electron Transfer

Shijian Jin[†], Min Wu[†], Roy Gordon[‡], Michael J. Aziz[†*] and David G. Kwabi[†§]

[†] John A. Paulson School of Engineering and Applied Sciences, Harvard University, Cambridge, Massachusetts, 02138, United States

[‡]Department of Chemistry and Chemical Biology, Harvard University, Cambridge, Massachusetts 02138, United States

*maziz [at] harvard [dot] edu
[§]Present address: Department of Mechanical Engineering, University of Michigan, Ann Arbor MI 48109 USA. dkwabi [at] umich [dot] edu

Table of Figures

Table of Sections

Table of Tables

Table S1. Table of acronyms

Acronyms	Explanation
AEM	anion exchange membrane
AHP	2-amino-3-hydroxyphenazine
BHPC	benzo[a]hydroxyphenazine-7/8-carboxylic acid
CCS	carbon capture and sequestration
CEM	cation exchange membrane
DAC	direct air capture
DHPS	Phenazine dihydroxysulfonic acid
DIC	dissolved inorganic carbon
DSPZ	sodium 3,3'-(phenazine-2,3-diylbis(oxy))bis(propane-1-sulfonate)
EMAR	electrochemically mediated amine regeneration
HP	2-hydroxyphenazine
MEA	monoethanolamine
PCET	proton-coupled electron transfer
RFB	redox-flow batteries
TA	total alkalinity

Thermodynamic Analysis

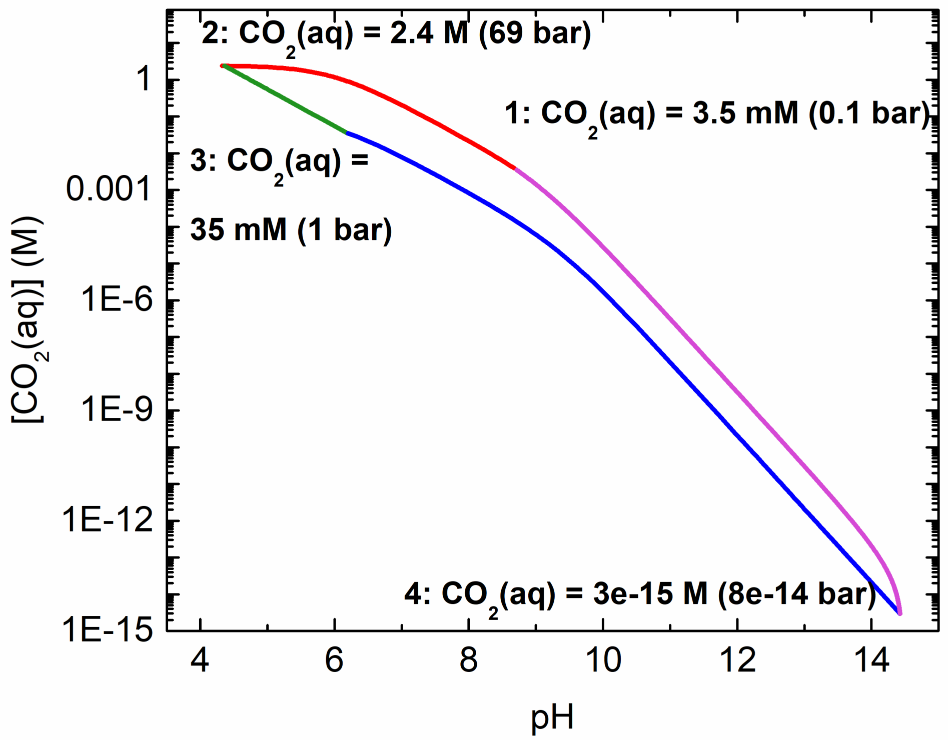

Figure S1. CO$_2$(aq) vs. pH during the 4-process cycle described in **Figure 4**. Processes 1→2 and 2→3 are depicted with red lines, and processes 3→4 and 4→1 are depicted in blue lines. The equilibrium CO$_2$ pressure corresponding to each CO$_2$(aq) is stated.

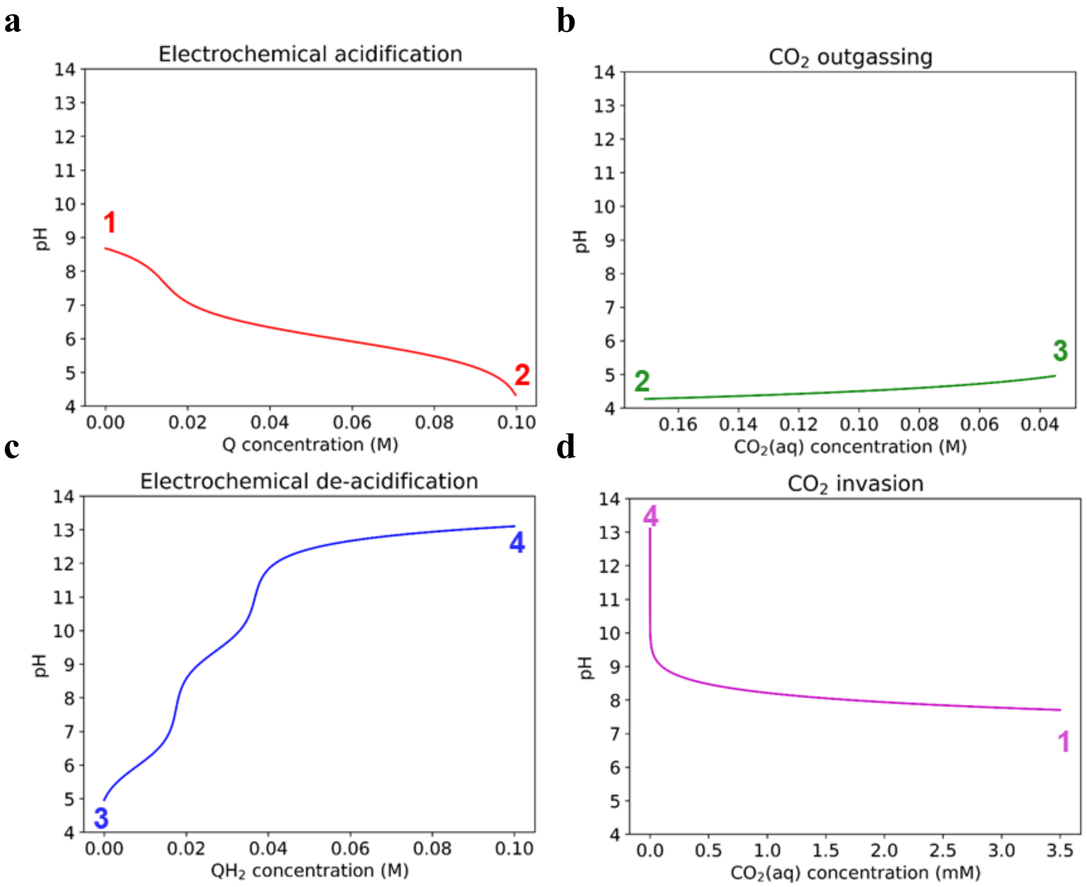

Figure S2. Ideal CO_2 separation cycle for starting QH_2 concentration of 0.1 M, DIC concentration of 0.175 M and an exit/inlet pressure ratio of 10, which translates to an outgassing overpressure of 5. pH as a function of Q and QH_2 concentration and $CO_2(aq)$ during (a) electrochemical acidification (process 1 → 2) (b) CO_2 outgassing (process 2 → 3) (c) electrochemical de-acidification (process 3 → 4) and (d) CO_2 invasion (process 4 → 1), at the end of which aqueous CO_2 ($CO_2(aq)$) is assumed to be in equilibrium with 0.1 bar CO_2 gas.

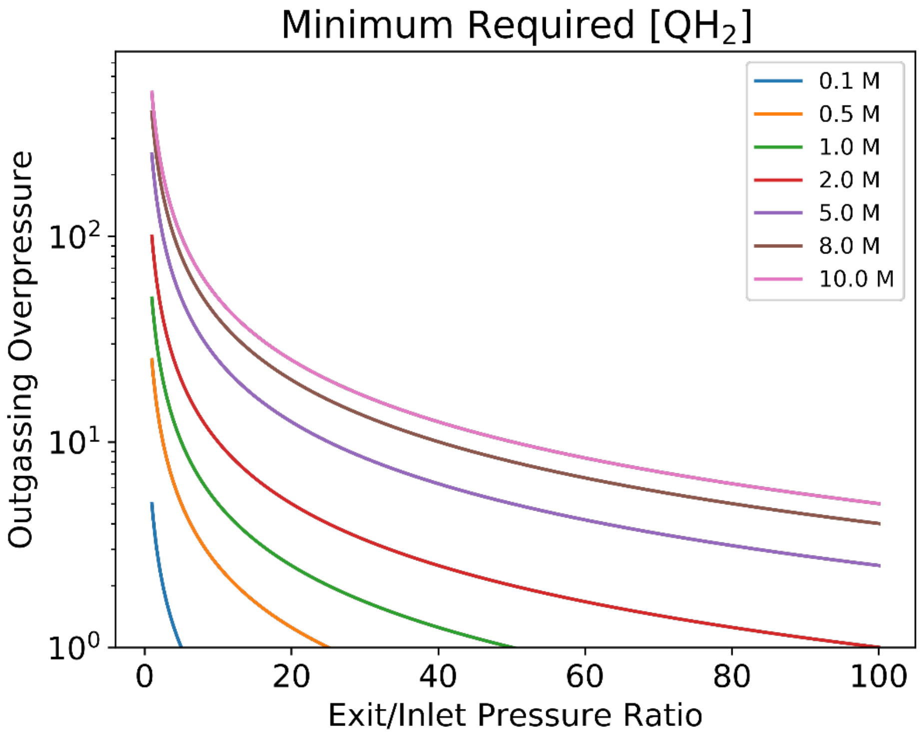

Figure S3. Relationship between outgassing overpressure and exit/inlet pressure ratio for various [QH_2] values at State 1 between 0.1 and 8.0 M, assuming the solution at State 1 is in equilibrium with 0.1 bar CO_2 gas.

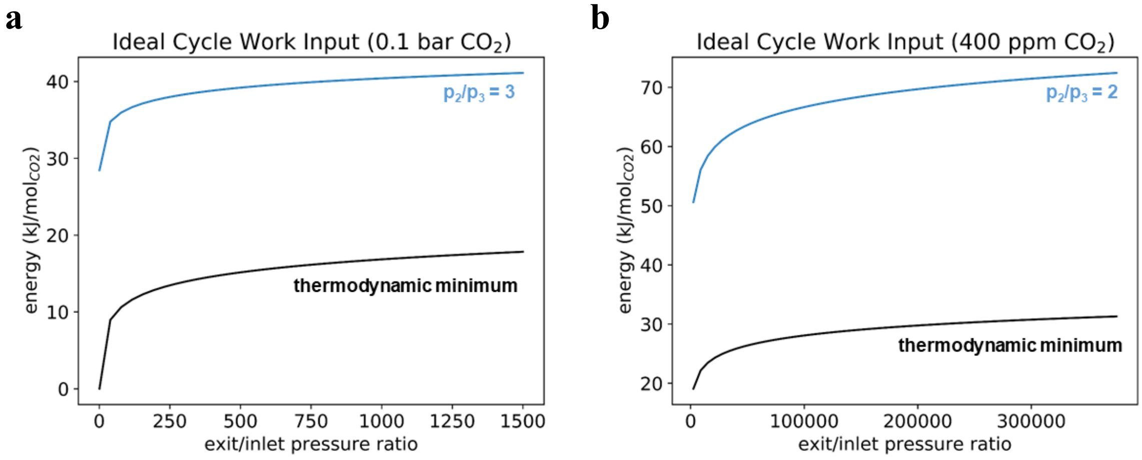

Figure S4. Ideal cycle work vs exit/inlet pressure ratios for inlet streams at (a) 0.1 bar and (b) 400 ppm CO_2. The highest exit/inlet pressure ratio represents an exit pressure of 150 bar $CO_2(g)$, and the maximum overpressure plotted in each case is based on the assumption that QH_2 concentration can reach up to 10 M.

1 *Estimation of Final pH after Electrochemical De-acidification.*

The relative concentration of protonated/deprotonated reduced Q is given by the Henderson-Hasselbalch equation, which relates solution pH to the pKa of QH_2 and the concentrations:

$$pH = pK_a + log_{10}\frac{[Q^{2-}]}{[QH_2]}. \text{ eq. S 1}$$

By assuming that each mole of QH_2 created by the bulk electrolytic reduction of a mole of Q removes 2 moles of H^+ from solution, we can calculate the final pH of a given solution given its initial pH, the concentration of Q, and the pK_a of Q. The final pH is given by:

$$pH = 14 - pOH, \text{ eq. S 2}$$

where *p*OH is defined based on the logarithmic constant for OH^- concentration, as $-\log_{10}[OH^-]$. Because the final pH is the sum of the initial OH^- concentration and OH^- ions created by electrochemical reduction of Q, we may re-write the above equation as:

$$pH = 14 + log_{10}(OH_0^- + OH_n^-), \text{ eq. S 3}$$

where OH_0^- is the initial OH^- concentration and OH_n^- represents newly created OH^-. Based on the Henderson-Hasselbalch equation, one can re-express solution pH as a function of starting reactant concentration Q and its protonated reduced form, QH_2:

$$10^{(pH-pK_a)} = \frac{[Q^{2-}]}{[QH_2]} = \frac{[Q-QH_2]}{[QH_2]} = \frac{[Q]}{[QH_2]} - 1. \text{ eq. S 4}$$

By re-arranging terms and assuming that the formation of each new QH_2 produces two OH^- ions, we obtain an expression for OH_n^-:

$$OH_n^- = \frac{2Q}{1+10^{(pH-pK_a)}}. \text{ eq. S 5}$$

Plugging this expression for OH_n^- into eq. S1 provides the full relationship between solution pH, pK_a, initial pH and Q concentration:

$$pH = 14 + log_{10}\left(10^{(pH_0-14)} + \frac{2Q}{1+10^{(pH-pK_a)}}\right). \text{ eq. S 6}$$

The plot below depicts final pH upon full reduction of Q as a function of pKa for a solution with initial pH 3 and a series of Q concentrations ranging from 50 mM to 2.0 M.

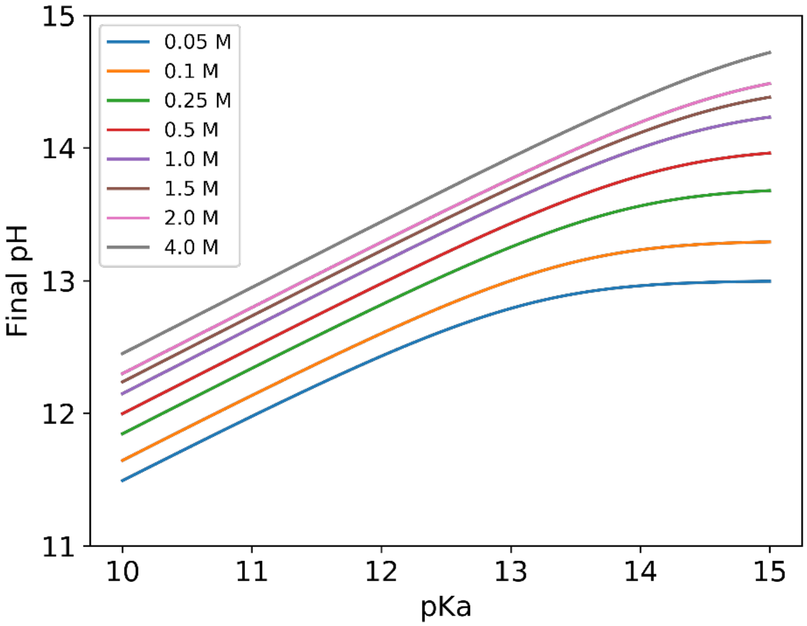

Figure S5. Relationship between pKa of *Q* and final pH upon reduction of *Q* based on the solution to implicit equation S6 for a series of *Q* concentrations between 50 mM and 2.0 M.

It is important to note two assumptions that have been made: (1) the solution is completely unbuffered; and (2) *Q* has one pKa at which protons are in equilibrium with its deprotonated reduced form. As has been shown in the RFB literature, this is the case for some redox-active species (such as 2,6-dihydroxyanthraquinone [1]) but is not generally true for all reactants capable of PCET, which may have two distinct pKa values for each proton.[2] The main consequence of these assumptions is that the final pH computed above represents an upper limit, as buffering effects will reduce the power of PCET to effect pH shifts, and the presence two distinct pKa values imply a regime in which two-electron reduction will be accompanied by removal of one rather than two protons from solution.

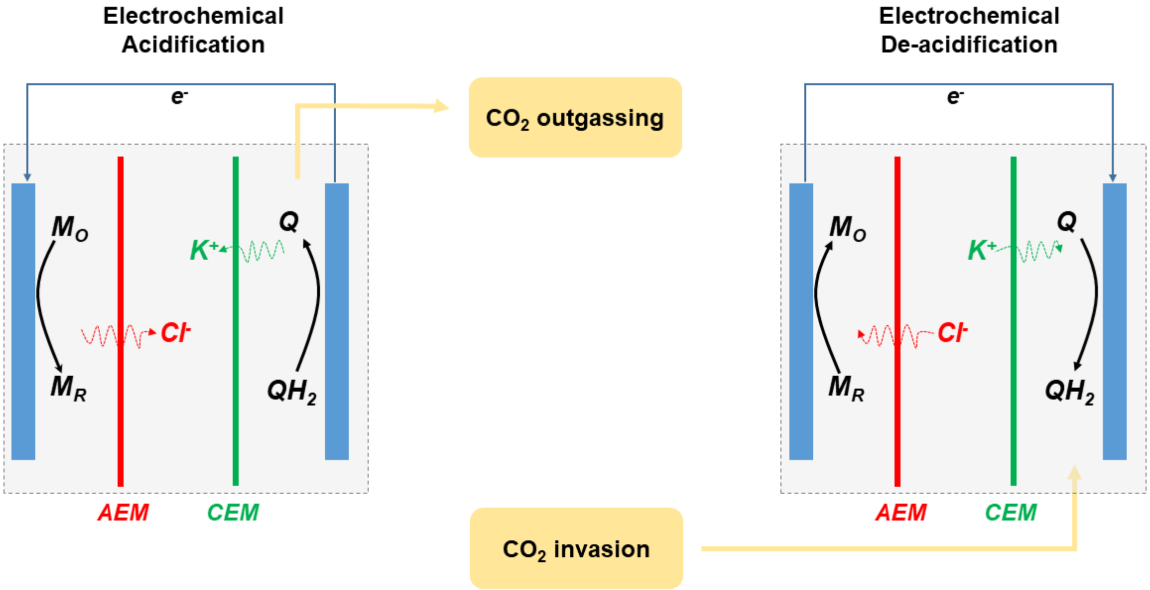

Figure S6. Schematic of two-membrane electrochemical cell, showing how electrochemical acidification and de-acidification processes are integrated with CO_2 outgassing and invasion. A KCl supporting salt is assumed, and K^+ and Cl^- ions move through the CEM and AEM, respectively, to/from a middle electrolyte chamber. M_O and M_R, represent the redox processes occurring counter to Q/QH_2, and could be either symmetric (i.e. QH_2/Q) or asymmetric (i.e. employing some other redox couple), the latter case implying that CCS could be integrated with energy storage.

Experimental

2 *Synthesis and Characterization*

All chemicals were purchased from Sigma-Aldrich or Acros Organics unless specified otherwise. All chemicals were used as received unless specified otherwise.

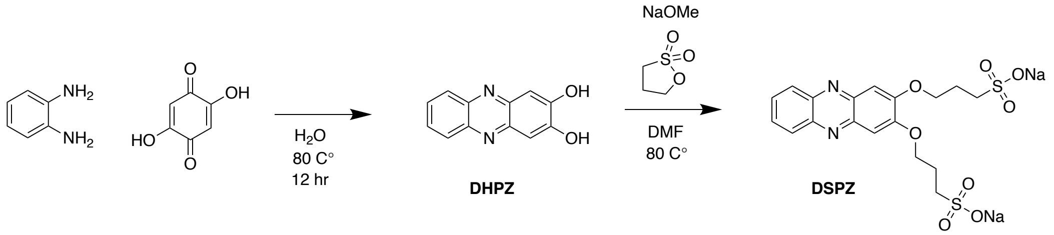

Scheme S1. Synthesis of 1,1'-bis(3-phosphonopropyl)-[4,4'-bipyridine]-1,1'-diium dibromide (DSPZ)

benzene-1,2-diamine (1 equiv.) was mixed with 2,5-dihydroxycyclohexa-2,5-diene-1,4-dione (1.03 equiv.) in water to achieve 0.2 M benzene-1,2-diamine solution in a pressure vessel. The reaction mixture was refluxed at 80 °C and stirred overnight. The resulting slurry was filtered and the black precipitate was crude product phenazine-2,3-diol (DHPZ). The black precipitate was then dissolved in 0.1 M KOH solution to make a 0.02 M DHPZ solution. The solution was filtered again and the filtrate was acidified with HCl solution until pH 7. Red precipitates formed and were filtered to give pure DHPZ (99% yield).

DHPZ (1 equiv.) was dissolved in DMF to make 0.1 M DHPZ solution. A methanoal solution of sodium methoxide (3 equiv. NaOMe) was added to the DHPZ solution under N_2. 2.5 equiv. propane sultone was then added into the solution. The reaction mixture was stirred overnight at 80 °C to give an red slurry. The slurry was then cooled and filtered. The red precipitates were washed thoroughly with ethyl acetate to remove residual DMF. The final DSPZ products were red solids (88% yield)

DSPZ: ^1H NMR (500 MHz, D_2O) δ 7.40-7.48 (m, 2H), 7.22-7.27 (m, 2H), 5.84 (s, 2H), 3.65-3.75 (m, 4H) , 3.03-3.09 (m, 4H), 2.12-2.22 (m, 4H),

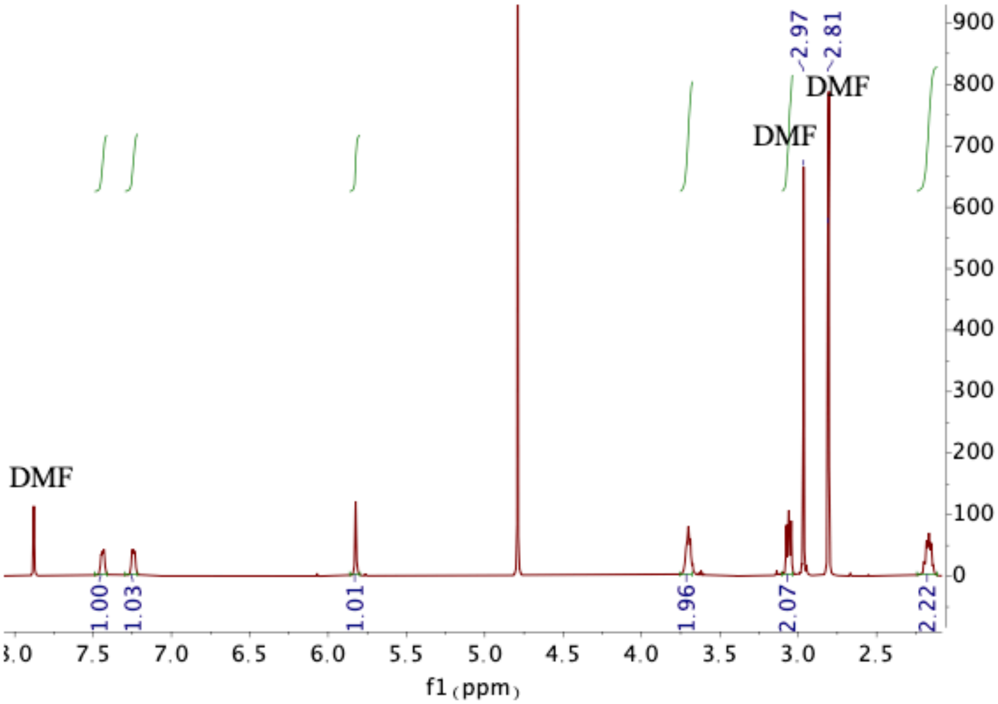

Figure S7. 1H NMR spectrum of DSPZ in DMSO-d6. The solvent DMF remained in the solution.

The solubility of DSPZ was measured using UV-Vis spectroscopy. A calibration line was obtained using the absorption peak at 395 nm of 10, 20, 40 and 50 µM DSPZ solutions. An aliquot of saturated DSPZ solution (in 1 M KCl or KOH, with 1 vol% anti-foam agent) was diluted 20,000 times, and then the absorption spectrum of the diluted solution was measured. The calculated solubility values for DSPZ in 1 M KCl (pH = 5.9) and in 1 M KOH (pH =14) are both 0.73 M. **Figure S8** shows the calibration line and the absorbance of the 20,000 times diluted saturated solution.

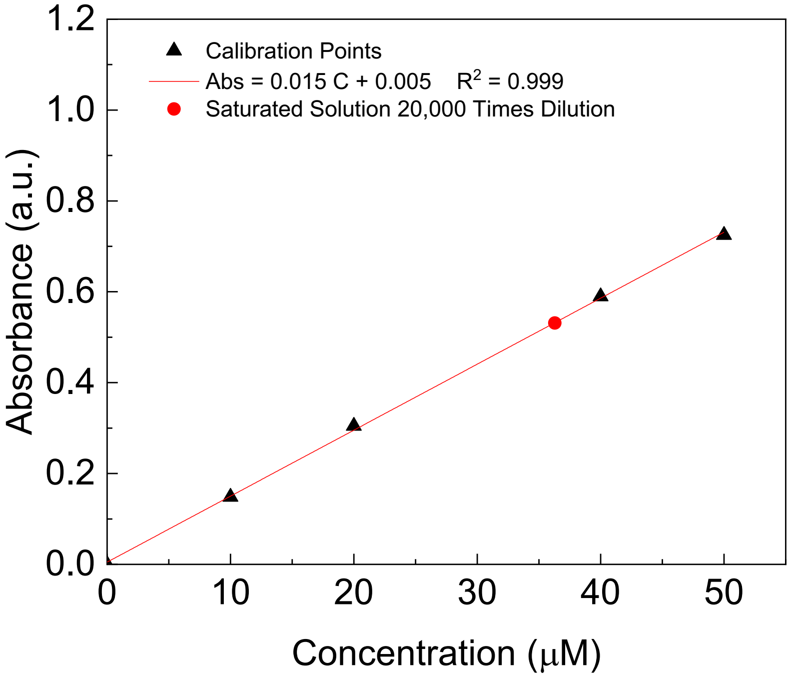

Figure S8. Calibration line and the measured solubility (0.73 M at pH 6.8 and 14) of DSPZ.

3 *Electrochemistry*

Glassy carbon (BASi MF-2012, 3.0mm diameter) was used as the working electrode for all three-electrode CV tests. A Ag/AgCl reference electrode (BASi MF-2052, pre-soaked in 3 M NaCl solution), and a graphite counter electrode were used for CV tests. CV tests and cell cycling were performed using a Gamry Reference 3000 potentiostat. 0.1 mL of antifoam B emulsion purchased from Sigma-Aldrich was added into the negolyte solution before cell cycling in order to prevent foam formation.

Flow cell experiments were constructed with cell hardware from Fuel Cell Tech. (Albuquerque, NM), assembled into a zero-gap flow cell configuration, similar to a previous report.[1] Pyrosealed POCO graphite flow plates with serpentine flow patterns were used for both electrodes. Each electrode comprised a 5 cm^2 geometric surface area covered by a stack of four sheets of Sigracet SGL 39AA porous carbon paper pre-baked in air for 24 h at 400 °C. The specific area of SGL 39AA carbon paper is 0.5 m^2/g, as reported by Forner-Cuenca *et al.*[3] The outer portion of the space between the electrodes was gasketed by Viton sheets with the area over the electrodes cut out. Torque applied during cell assembly was 60 lb-in on each of 8 bolts. Posolytes were fed into the cell through fluorinated ethylene propylene (FEP) tubing at a rate of 100 mL/min controlled by a Cole-Parmer 6 Masterflex L/S peristaltic pump, and the negolytes were circulated at the same rate controlled by a Cole-Parmer Masterflex digital benchtop gear pump system. The flowmeter used in the gas outlet was a Honeywell AWM3150V. The CO_2 sensor was an ExplorIR-W 100% CO_2 sensor purchased from co2meter.com. Gases exited the negolyte chamber and reached the CO_2 sensor via a 10 cm FEP tubing with 1/16’’ ID. As shown in **Figure 9**, a drierite drying tube (Cole Parmer) and the flowmeter were in between the CO_2 sensor and the negolyte chamber, along the gas path. It took ~220 seconds for the gases at 10 mL/min to reach the CO_2 sensor from the negolyte chamber.

4 CO_2 Capture from 0.465 bar and Release to 1 bar

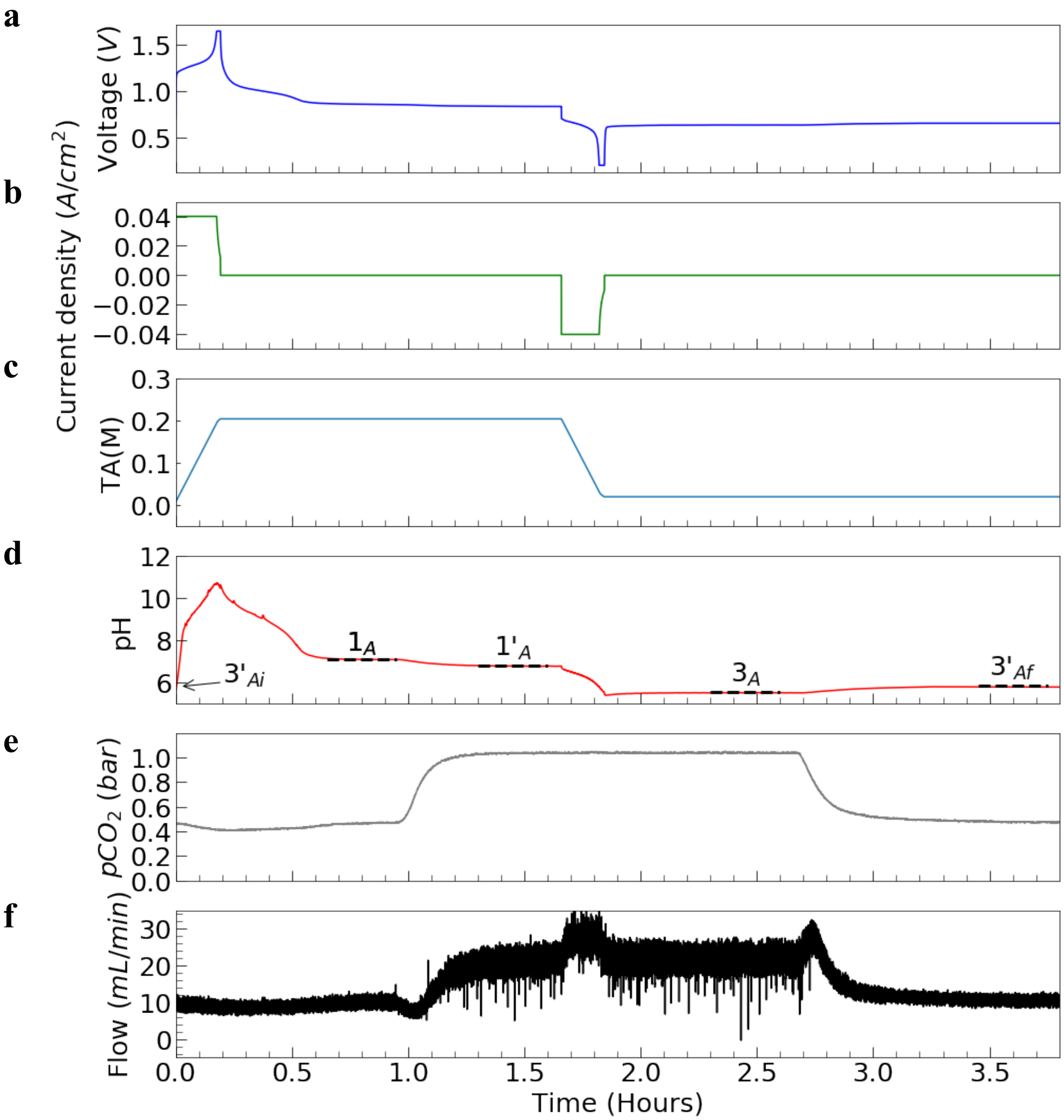

Figure S9 The concentrating cycle A**.** One full CO_2 capture/release cycle with 0.465/1 bar inlet/exit pressure using a DSPZ based flow cell at 40 mA/cm^2. Electrolytes comprised 7 mL 0.09 M DSPZ in 1 M KCl (negolyte, capacity limiting side, theoretical capacity = 121.6 C) and 40 mL of 0.1 M $K_4Fe(CN)_6$ and 0.1 M $K_3Fe(CN)_6$ in 1 M KCl (posolyte, non-capacity limiting side) (a) Voltage profile. (b) Current density. (c) Estimated total alkalinity. (d) pH. States 3'$_{Ai}$, 1$_A$, 1'$_A$, 3$_A$ and 3'$_{Af}$ represent pH values before deacidification under 0.465 bar pCO_2, after deacidification/absorption under 0.465 bar pCO_2, after changing pCO_2 from 0.465 bar to 1 bar, after acidification/desorption under 1 bar and after changing pCO_2 from 1 bar to 0.465 bar, respectively. (e) CO_2 partial pressure. (f) Total gas flow rate. Note that the gas flow rate undergoes large fluctuations between 1.2 and 2.6 hour.

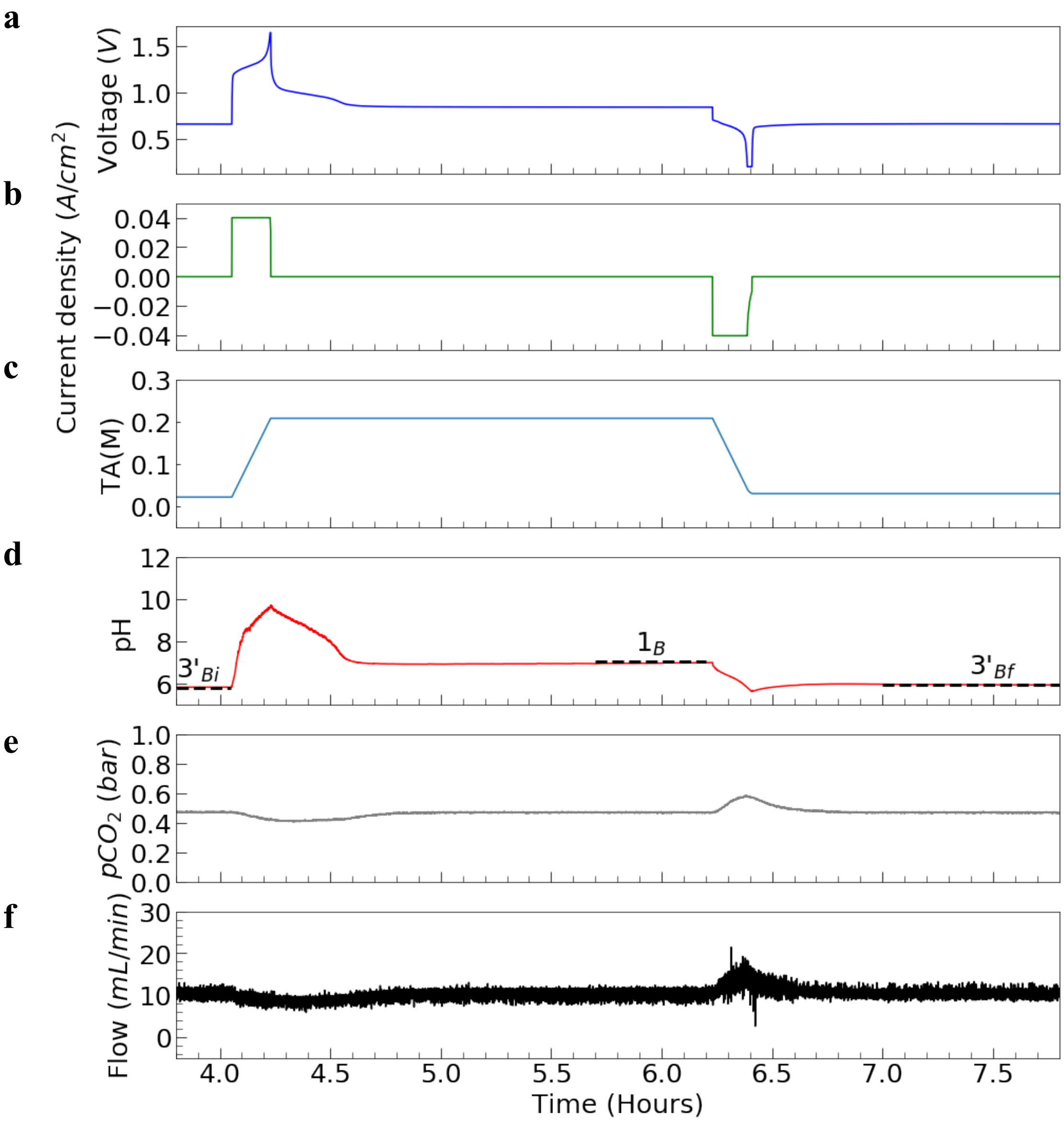

Figure S10. The non-concentrating cycle B. One full CO_2 capture/release cycle with 0.465/0.465 bar inlet/exit pressure using the same cell as in **Figure S9**. (a) Voltage profile. (b) Current density. (c) Estimated total alkalinity. (d) pH. $3'_{Bi}$, 1_B, and $3'_{Bf}$ represent pH values before deacidification under 0.465 bar pCO_2, after deacidification/absorption under 0.465 bar pCO_2 , and after acidification/desorption under 0.465 bar pCO_2, respectively. (e) CO_2 partial pressure. (f) Total gas flow rate.

Figure S9 demonstrates a CO_2 separation cycle where deacidification/CO_2 invasion take place at pCO_2 = 0.465 bar and acidification/CO_2 release take place at pCO_2 = 1 bar. **Figure S10** shows a subsequent cycle where both deacidification/CO_2 invasion and acidification/CO_2 release take place at pCO_2 = 0.465 bar. We refer to the former cycle as concentrating cycle A and the latter cycle as non-concentrating cycle B. In concentrating cycle A, we adjusted the nominal pCO_2 from

0.465 to 1 bar at the end of CO_2 invasion about ~ 55 minutes after the start of the experiment (**Figure S9**). This adjustment took about 20 minutes to complete and resulted in large fluctuations in gas flow rate (**Figure S9**f**,** 0.9 - 1.2 hour). Similarly long transient behavior took place again at the end of CO_2 release when we adjusted pCO_2 back to 0.465 bar (**Figure S9**e and f**,** 2.7 - 3.0 hour). These large fluctuations and long transients make the calculation of CO_2 absorbed or released via eq. 13 difficult. Therefore, for both cycles, we estimated DIC values using pH values at states $3'_{Ai}$ to $3'_{Af}$ (**Figure S9**d), TA and eq. 5-10. Note that states 3_A and 1_A in concentrating cycle A correspond to states 3 and 1 in **Figure 5** and **Figure 6**, except for higher pCO_2 and lower concentration of redox-active molecules. States $3'_A$ and $1'_A$ are similar to the corners part way through the two-stage acidification and two-stage deacidification processes in **Figure 5** and **Figure 6**. The difference is that DIC is kept constant from states 3 or 1 to the corners in **Figure 5** and **Figure 6**, whereas TA is kept constant from states $3_A/1_A$ to $3'_A/1'_A$ in the concentrating cycle A. Due to possible side reactions and/or inaccuracy in pH measurement, the initial $3'_A$ and final $3'_A$ states have slightly different pH values. Therefore, we add the subscripts "i" and "f" to denote the initial and final $3'_A$ states. The same nomenclature applies to the states in non-concentrating cycle B. We estimated DIC values under either of two assumptions. "DIC_{TA}" denotes values calculated under the assumption that TA changed only due to crossover of conservative ions (i.e. K^+ and Cl^-), rather than OH^-, H^+, HCO_3^-, CO_3^{2-} or redox-active molecules. We calculated "DIC_{eq}" values assuming that gas-solution equilibrium was achieved at all states. The results are summarized in **Table S2** and **Figure S11**.

Table S2 Summary of pCO_2, pH, TA, DIC_{TA} and DIC_{eq} in concentrating cycle A and non-concentrating cycle B.

States	pCO_2(bar)	pH	TA (M)	DIC_{TA} (M)	DIC_{eq}(M)
$3'_{Ai}$	0.465	5.6	0.0066	0.0229	0.0229
1_A	0.465	7.1	0.1867	0.200	0.233
$1'_A$	1	6.8	0.1867	0.214	0.268
3_A	1	5.5	0.0067	0.0253	0.0475
$3'_{Af}$	0.465	5.8	0.0067	0.0167	0.0271
$3'_{Bi}$	0.465	5.8	0.0067	0.0167	0.0271
1_B	0.465	7.1	0.1867	0.199	0.233
$3'_{Bf}$	0.465	5.8	0.0067	0.0158	0.0280

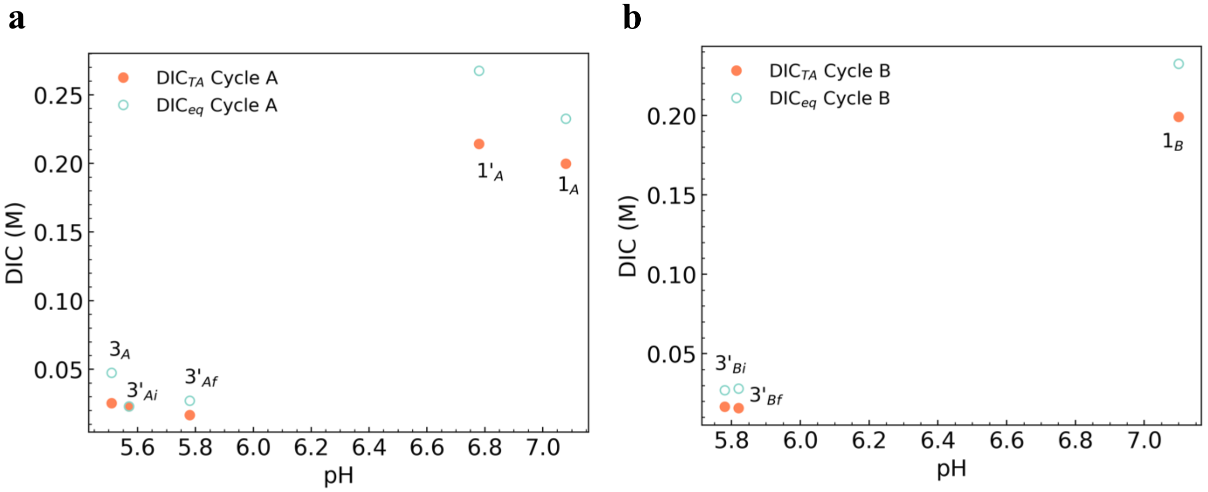

Figure S11 DIC versus pH in (a) concentrating cycle A and (b) non-concentrating cycle B.

Table S3 Summary of ΔDIC_{TA}, ΔDIC_{eq} , $\Delta DIC_{measured}$ and work input for different processes.

Process Nomenclature	Initial State	Final State	Process	ΔDIC_{TA} (M)	ΔDIC_{eq} (M)	$\Delta DIC_{measured}$ (M)	Work Input (J)
$\Delta DIC_{A3'1}$	$3'_{Ai}$	1_A	Deacidification/ Capture	0.177	0.210	NA	176.6
ΔDIC_{A13}	1_A	3_A	Acidification/ Release	-0.174	-0.185	NA	-73.8
$\Delta DIC_{A13'}$	1_A	$3'_{Af}$	Acidification/ Release	-0.183	-0.206	NA	-73.8
$\Delta DIC_{B3'1}$	$3'_{Bi}$	1_B	Deacidification/ Capture	0.182	0.206	0.186	173.5
$\Delta DIC_{B13'}$	1_B	$3'_{Bf}$	Acidification/ Release	-0.183	-0.205	0.190	-74.7

In concentrating cycle A, the amount of CO_2 captured at 0.465 bar is $\Delta DIC_{TA,A3'1}$, i.e. the difference between DIC values at $3'_{Ai}$ and 1_A, when no crossover of non-conservative ions is assumed, or $\Delta DIC_{eq,A3'1}$ when equilibrium is assumed. Neglecting the increment of CO_2 absorbed upon changing pCO_2 from 0.465 to 1 bar, the total amount of CO_2 captured at 0.465 bar and released at 1 bar is $\Delta DIC_{TA,A13}$ or $\Delta DIC_{eq,A13}$., whereas $\Delta DIC_{TA,\ A13'}$ or $\Delta DIC_{eq,A13'}$ represent the sum of $\Delta DIC_{TA,A13}$ or $\Delta DIC_{eq,A13}$ and the amount of CO_2 released after pCO_2 is changed to 0.465 bar. In non-concentrating cycle B, the amount of CO_2 captured estimated from pH and TA is $\Delta DIC_{TA,B3'1}$ or $\Delta DIC_{eq,B3'1}$ and the amount of CO_2 released is $\Delta DIC_{TA,B13'}$ or $\Delta DIC_{eq,B13'}$. Because no transients occurred during non-concentrating cycle B, we also measured the amount of CO_2 captured or released via eq. 13 and denoted those values $\Delta DIC_{measured}$. **Table S3** summarizes ΔDIC_{TA}, ΔDIC_{eq}, $\Delta DIC_{measured}$ and work input, calculated using eq. 15, of the relevant processes. We note that $\Delta DIC_{measured}$ is on average only 3% higher than ΔDIC_{TA} but 8.5% lower than ΔDIC_{eq}; this result suggests that during non-concentrating cycle B crossover of non-conservative ions is insignificant. Note that $\Delta DIC_{TA,A13'}$ of concentrating cycle A is the same as $\Delta DIC_{TA,B13'}$ of non-concentrating cycle B, suggesting that the net amount of CO_2 released to 0.465 bar is the same whether it is released directly to a pCO_2 of 0.465 bar, or is first released to 1 bar before a pCO_2 of 0.465 bar is imposed. We expect less CO_2 to remain dissolved in solution after CO_2 release at a CO_2 partial pressure of 0.465 bar than after release at 1 bar; based on **Table S3**, 5–10% less CO_2 is released, depending on whether we assume full gas-solution equilibration or no crossover of non-conservative ions. For concentrating cycle A, the net cycle work is 102.8 J, which translates to 79.4 and 84.2 kJ/mol_{CO2} corresponding to ΔDIC_{TA} and ΔDIC_{eq}, respectively. For non-concentrating cycle B, the net cycle work is 98.8 J, which translates to 75.1 kJ/mol_{CO2}, using $\Delta DIC_{measured}$. Therefore, the work input for concentrating CO_2 from 0.465 to 1 bar is between 4.3 and 9.1 kJ/mol_{CO2} higher than that for CO_2 capture from and release to 0.465 bar. This value is two to five times higher than the limit from thermodynamic considerations (1.9 kJ/mol_{CO2}) but is small relative to our estimates of actual work input for CO_2 capture and release at 40 mA/cm^2, which range between 75.1 and 84.2 kJ/mol_{CO2}.

As mentioned in the **Discussion** section, part of the net cycle work overcomes cell overpotential, while the remainder is associated with CO_2 capture and release. We measured the former by cycling the same cell prior to cycles A and B under N_2 (i.e. no CO_2 capture and release) at 40 mA/cm^2 and obtained a cycle work of 61.3 J. The difference between this figure and the cycle work in concentrating cycle A is 41.5 J, which, in combination with ΔDIC_{eq} or ΔDIC_{TA}, yields an actual work input dedicated only to CO_2 capture and release of 32.0 or 34.1 kJ/mol$_{CO2}$, respectively for an exit/inlet ratio 1/0.465.

5 *Estimate of Activation Overpotential*

The total cycle activation overpotential is the difference between deacidification overpotential and acidification overpotential, i.e.:

$$\eta_{total} = \eta_{deacidification} - \eta_{acidification} \quad eq.\ S\ 7$$

where $\eta_{deacidification}$ and $\eta_{acidification}$ each have cathodic and anodic components:

$$\eta_{cathodic} = \frac{RT}{\alpha nF} \ln \frac{i_0}{|i|} \quad eq.\ S\ 8$$

$$\eta_{anodic} = \frac{RT}{(1-\alpha)nF} \ln \frac{|i|}{i_0} \quad eq.\ S\ 9$$

where η is the activation overpotential, R is the ideal gas constant 8.314 J/mol K, T is the temperature 293.15 K and F is the Faraday's constant of 96,485 Coulomb/mol. α is the transfer coefficient of the redox couple, n is the number of electrons transferred per reactant molecule, i_0 is its exchange current density and i is the applied current. i_0 is calculated by:

$$i_0 = nAFk^0 Conc. \quad eq.\ S\ 10$$

where k^0 is the standard heterogeneous rate constant and *C*onc. is the concentration of the oxidized form of the electrolyte at 1:1 ratio of [oxidized form]:[reduced form], or a state of charge of 50%, and A is the electrode surface area, in our case 500 cm^2 for 4 sheets of SGL39 AA porous carbon paper electrodes, each of 5 cm^2 geometric surface area and 125 cm^2 surface area, assuming the specific area of SGL 39AA carbon paper is 0.5 m^2/g.[3]

For deacidification, the participating half reactions are :

$$\text{Anodic: } Fe(CN)_6^{4-} \rightarrow Fe(CN)_6^{3-} + e^- \quad eq.\ S\ 11$$

$$\text{Cathodic: } DSPZ + 2e^- + 2H_2O \rightarrow DSPZH_2 + 2OH^- \quad eq.\ S\ 12$$

For acidification, the participating half reactions are:

$$\text{Cathodic: } Fe(CN)_6^{3-} + e^- \rightarrow Fe(CN)_6^{4-} \quad eq.\ S\ 13$$

$$\text{Anodic: } DSPZH_2 + 2OH^- \rightarrow DSPZ + 2e^- + 2H_2O \quad eq.\ S\ 14$$

Because the $Fe(CN)_6^{4-}/Fe(CN)_6^{3-}$ and $DSPZ/DSPZH_2$ redox couples are present in the posolyte and negolyte, respectively,

$$\eta_{deacidification} = \eta_{anodic,Fe} - \eta_{cathodic,DSPZ} \quad eq.\ S\ 15$$

$$\eta_{acidification} = \eta_{cathodic,Fe} - \eta_{anodic,DSPZ} \quad eq.\ S\ 16$$

For the DSPZ-containing negolyte, we estimated the activation overpotentials at the experimental currents of 200, 250, 375, 500, 625 and 750 mA based on $k^0 = 1.47 \times 10^{-2} cm/s$ and $\alpha = 0.4$, as reported by Xie *et al*, because of the similar structures of DSPZ and DHPS.[4] *Conc.* is 0.039 M at 50% state of charge and n is 2. The calculated i_0 for DSPZ/DSPZH$_2$ is 55 mA. The resulting $\eta_{cathodic,DSPZ}$ at the experimental currents are −41, −48 , −60, −70, −77 and −82 mV, respectively and $\eta_{anodic,DSPZ}$ at the experimental currents are 27, 32, 40, 46, 51 and 55 mV, respectively. For the posolyte side, we estimated the activation overpotential using reported ferrocyanide/ferricyanide $k^0 = 1.5 \times 10^{-2}$ cm/s and $\alpha = 0.5$ reported by Angell *et al.*[5] *Conc.* is 0.1 M at 50% state of charge and n is 1. The calculated i_0 for $Fe(CN)_6^{4-}/Fe(CN)_6^{3-}$ couple is 72 mA/cm^2. The resulting $\eta_{anodic,Fe}$ at the experimental currents are 51, 63, 83, 98, 109, and 118 mV, respectively and the resulting $\eta_{cathodic,Fe}$ at the experimental currents are −51, −63, −83, −98, −109, and −118 mV, respectively. These values and the corresponding $\eta_{deacidification}$ and $\eta_{acidification}$ values are summarized in **Table S 4**.

Table S4. Estimated activation overpotentials at various currents*

Current/Components	200 mA	250 mA	375 mA	500 mA	625 mA	750 mA
$\eta_{anodic,Fe}$	51	63	83	98	109	118
$\eta_{cathodic,DSPZ}$	−41	−48	−60	−70	−77	−82
$\eta_{deacidification}$	92	110	144	167	185	200
$\eta_{cathodic,Fe}$	−51	−63	−83	−98	−109	−118
$\eta_{anodic,DSPZ}$	27	32	40	46	51	55
$\eta_{acidification}$	−78	−95	−123	−144	−160	−173

*Units in mV

Using $\eta_{deacidification}$ and $\eta_{acidification}$ values with absolute values above 118 mV, we linearly extrapolate to zero current and obtain an η_{total} of 165 mV.The electrical work associated with the cell activation overpotential is

$$w = \eta_a q, \quad eq.\ S\ 17$$

where q is the cell capacity required for capturing/releasing 1 mol CO$_2$ and can be calculated by

$$q = \frac{nF}{r}, \quad eq.\ S\ 18$$

where r is the ratio of ΔDIC to DSPZ concentration (in this case 0.158/0.078 because 0.078 M DSPZ was able to capture enough CO$_2$ to make a solution with 0.158 M ΔDIC), and $n = 2$ because DSPZ undergoes a 2-electron process. We obtained a cell capacity of 140000 C and an electrical work of 15.7 kJ/mol$_{CO2}$.

Note that deviations from this value could take place because of several factors including but not limited to:

1. The rate constants were measured with glassy carbon or metal electrodes whereas carbon paper electrodes were used in the experiments;
2. The rate constants were measured in a solution with no anti-foam agent whereas anti-foam agent was present in the experiments;

3. The rate constants were measured at a specific pH whereas the experiments covered a range of pH values;
4. Based on the large peak separation displayed on the CV diagrams (**Figure 8**c), DSPZ is likely to have more sluggish kinetics and hence possess a smaller rate constant than DHPS. In order for the estimate above to yield 32 kJ/mol$_{CO2}$ electrical work instead of 15.7 kJ/mol$_{CO2}$, the kinetic constant of DSPZ would have to be ~ 1×10^{-4}cm/s, which is a reasonable value compared to the rate constants of other organic redox active molecules used in a flow cell;
5. The electrode active area was calculated based on previous literature[3], but different electrode pretreatment could result in different active area.

6 Estimate of CO_2 Kinetic Losses

The ideal cycle work for the four-process CO_2 separation cycle depends on the exit/inlet pressure ratio (p_3/p_1) and the CO_2 outgassing overpressure (p_2/p_3)(**Figure 7**). For the experimental conditions outlined in **Figure 10**, the exit/inlet pressure ratio for absorbing CO_2 from a gas stream with 0.465 bar CO_2 partial pressure and release to 1.0 bar CO_2 is 2.17. The CO_2 outgassing overpressure is 5.54 if [CO_2 (aq)] after acidification is 0.159 M. Using these values and the same program that generated **Figure 7**, we obtain an ideal cycle work of 34 kJ/mol$_{CO2}$.

This calculation, however, assumes a four-process CO_2 separation cycle from 0.1 to 1 bar CO_2(g), whereas the experimental situation is arguably closer to the two-process CO_2 separation cycle shown by the dashed lines in **Figure 5** and **Figure 6**. A definition of the minimum electrochemical work that is readily applicable to these experimental conditions is the sum of the CO_2 kinetic losses, i.e. exergetic losses during CO_2 release and invasion, and the thermodynamic minimum work of separation. The total exergy lost during CO_2 release can be estimated as:

$$\bar{w} = RTln\frac{[\widetilde{CO}_2(aq)_{release}]}{[\,CO_2(aq)_{equilibrium}]} \quad eq.\ S\ 19$$

where $[\widetilde{CO}_2(aq)_{release}]$ is the average aqueous CO_2 concentration during outgassing, and $[\,CO_2(aq)_{equilibrium}]$ is the CO_2 concentration in local equilibrium with the head space, which in this case is the product of 0.465 bar and the Henry's Law constant of $3.5 \times\ 10^{-2}$ mol/(L bar), which yields 0.016 M. In the limit where the flow of gas in the cell headspace is infinitesimal, the increase in $[CO_2(aq)]$ above its steady-state value (e.g., in **Figure 10**) is proportional to the increase in CO_2 partial pressure in the headspace, i.e.

$$\Delta[CO_2(aq)] = \frac{\Delta p_{co2}}{RT}\frac{V_{headspace}}{V_{electrolyte}} \quad eq.\ S\ 20$$

where Δp_{co2} is the change in partial pressure of CO_2 in the headspace during CO_2 invasion or release, $V_{electrolyte}$ is the volume of the electrolyte (7 mL) and $V_{headspace}$ is the volume of the headspace (~ 50 mL). The average Δp_{co2} during CO_2 outgassing was 0.05 bar (**Figure 10**e) resulting in a $[\widetilde{CO}_2(aq)_{release}]$ of 0.031 M (i.e. 0.016 M + 0.015 M), and $\bar{w}$ of 1.6 kJ/mol$_{CO2}$. This figure, however, is an estimate of the lower limit of the exergy lost, as the flow rate of gas in the cell headspace is finite, and the measured Δp_{co2} would therefore be lower than that for the infinitesimal-flow limit for the same $\Delta[CO_2(aq)]$. We estimate the upper limit of the exergy lost by assuming that the increase in [CO_2(aq)] is equal to the DIC increase during CO_2 invasion, i.e. that all CO_2 that came in during invasion is present as supersaturated CO_2 before outgassing begins. Under these conditions, the numerator in eq. S19 is 0.159 M + 0.016 M, and the corresponding lost exergy is 5.8 kJ/mol$_{CO2}$. A reasonable estimate for the lost exergy is the average of the two estimates, which is 3.7 kJ/mol$_{CO2}$.

The exergy lost during CO_2 invasion, on the other hand, is the maximum amount of work that can be recovered from the reaction between OH^- and CO_2, and is the absolute value of the Gibbs free energy of the reaction, ΔG_R. In the present case,

$$\Delta G_R = \Delta G_R^O + RTln\,N, \quad eq.\ S\ 21$$

where

$$\Delta G_R^O = -RT\ln K_{eq}; \quad eq.\ S\ 22$$

K_{eq} is the equilibrium constant, and N is the average reaction quotient during CO_2 invasion. ΔG_R is therefore equal to $RT\ln\,(N/K_{eq}).N/K_{eq}$ is proportional to the ratio between the OH^- and aqueous CO_2 concentrations at equilibrium (i.e. 3.16×10^{-8} and 0.016 M), and the average OH^- and CO_2 concentrations during CO_2 invasion, $[\widetilde{\mathrm{CO}_2(\mathrm{aq})_{\mathrm{invasion}}}]$, which can be derived from pH measurements, and the relationship between Δp_{co2} and $\Delta[\mathrm{CO}_2(\mathrm{aq})]$ shown above, respectively. Given an average [OH^-] during invasion of 2.5×10^{-6} M and average CO_2 partial pressure during invasion of 0.42 bar, $[\widetilde{\mathrm{CO}_2(\mathrm{aq})_{\mathrm{invasion}}}]$ is 0.003 M (= 0.016 M – 0.013 M) and the corresponding exergy lost during CO_2 invasion is 6.6 kJ/mol$_{CO2}$ (**Figure 10**d and e). Because the thermodynamic minimum work of separation is zero here, the minimum electrochemical work input would be 10.3 kJ/mol$_{CO2}$.

Our estimate of the minimum electrochemical work input could be off because:

1. The average aqueous CO_2 concentration, instead of instantaneous CO_2 concentration, was used in the calculation;
2. Exergy losses are nonlinearly related to concentration;
3. The ratios $[\widetilde{\mathrm{HCO}_3^-}_{\mathrm{invasion}}]/[\mathrm{HCO}_3^-{}_{\mathrm{equilibrium}}]$ and $[\widetilde{\mathrm{CO}_3^{2-}}_{\mathrm{invasion}}]/[\mathrm{CO}_3^{2-}{}_{\mathrm{equilibrium}}]$ may deviate significantly from 1, as is implicitly assumed here.

Note that the above calculations neglect exergy losses from mixing between absorbed or released CO_2 and the 0.465 bar CO_2 reservoir, as these are external to the device itself.

7 Bibliography

1. K. Lin, Q. Chen, M. R. Gerhardt, L. Tong, S. B. Kim, L. Eisenach, A. W. Valle, D. Hardee, R. G. Gordon, M. J. Aziz and M. P. Marshak, *Science*, 2015, **349**, 1529.
2. C. Costentin, *Chem. Rev.*, 2008, **108**, 2145-2179.
3. A. Forner-Cuenca, E. E. Penn, A. M. Oliveira and F. R. Brushett, *Journal of The Electrochemical Society*, 2019, **166**, A2230-A2241.
4. H. Xie, Y. Wu, T. Liu, F. Wang, B. Chen and B. Liang, *Applied Energy*, 2020, **259**, 114119.
5. D. H. Angell and T. Dickinson, *J Electroanal Chem*, 1972, **35**, 55-72.